ROYAL SOCIETY
OF CHEMISTRY

COMMUNICATION

Check for updates

Full-visible transmissive metagratings with large angle/wavelength/polarization tolerance†

Zi-Lan Deng, [ID] *[a] Xuan Ye,[a] Hao-Yang Qiu,[b] Qing-An Tu,[a] Tan Shi,[a] Ze-Peng Zhuang,[b] Yaoyu Cao,[a] Bai-Ou Guan,[a] Naixing Feng,[c] Guo Ping Wang,[c] Polina Kapitanova,[d] Andrea Alù,[e] Jian-Wen Dong*[b] and Xiangping Li [ID] *[a]

Metagratings have been shown to form an agile and efficient platform for extreme wavefront manipulation, going beyond the limitations of gradient metasurfaces. Here, we present all-dielectric transmissive metagratings with high diffraction efficiencies using simple rectangular inclusions with neither high index nor high aspect ratio requirement. We further experimentally demonstrate continuous phase encoding of a hologram based on such transmissive metagratings through displacement modulation of CMOS-compatible silicon nitride nanobars in the full visible range, manifesting broadband and wide-angle high diffraction efficiencies for both polarizations. Featured with extreme angle/wavelength/polarization tolerance and alleviated structural complexity for both design and fabrication, our demonstration unlocks the full potential of metagrating-based wavefront manipulation for a variety of practical applications.

All-dielectric metasurfaces with discrete Mie scattering inclusions are recognized as an efficient platform to manipulate the light wavefront due to their negligible losses compared with plasmonic counterparts.[1] The geometric Pancharatnam–Berry phase[2,3] and the propagating phase[4] and their hybridization[5,6] have been widely employed in gradient metasurfaces to efficiently control the phase, polarization and amplitude profiles of light wavefront, leading to multifunctional planar optical devices such as high-performance metalenses,[7–10] high-quality meta-holograms,[11–19] tunable meta-devices[20,21] and nanoscale

color printings.[22–24] As there is a tradeoff between efficiency and spatial frequency bandwidth in gradient metasurfaces,[25,26] metagratings have emerged as an alternative platform to perform wavefront steering functionalities, especially for some extreme wavefront transformation scenarios.

In a metagrating, the scattering properties of identical inclusions in a periodic lattice are carefully tailored to achieve the desired diffraction order management, different from phase-gradient metasurfaces that employ a discrete set of different inclusions to map digitized phase levels in the 2π range. Guiding light towards a specified diffraction channel while suppressing all other diffraction orders has been the most popular application of metagratings so far. Metallic metagratings can easily achieve such high-efficiency single channel diffraction by tuning the plasmonic resonance in the extraordinary optical diffraction regime,[26,27] yet these approaches work better in reflection modes and their absolute efficiencies are hindered by intrinsic Ohmic losses.[28–37] Achieving single channel diffraction in all-dielectric transmissive metagratings is more challenging, as more diffraction channels coexist in both reflection and transmission semi-spaces. Usually, compound inclusions consisting of multiple dielectric scatters with specific asymmetric geometrics have been employed to achieve the near-perfect diffraction at the transmission side for normal incidence.[38–45] Due to the large duty-cycle, only limited phase profiles for beam bending and lensing have been demonstrated so far.[38–50] The structure requirements of metagratings are largely relaxed for oblique incidence,[51–54] yet previous reports did not achieve the perfect unitary diffraction, and their high diffractions are typically within a narrow angle range, a small bandwidth, and a sensitive polarization response, largely hindering their practical applications.

Here, we demonstrate an all-dielectric metagrating with high diffraction in the transmission side, enabling arbitrary and continuous spatial phase modulation independent of incident angle, wavelength and polarizations. The proposed metagrating is composed of simple rectangular inclusions with neither high refractive index nor high aspect ratio. The anomalous light channeling sustains robust high efficiency within a

[a]Guangdong Provincial Key Laboratory of Optical Fiber Sensing and Communications, Institute of Photonics Technology, Jinan University, Guangzhou 510632, China. E-mail: zilandeng@jnu.edu.cn, xiangpingli@jnu.edu.cn
[b]School of Physics and State Key Laboratory of Optoelectronic Materials and Technologies, Sun Yat-sen University, Guangzhou 510275, China. E-mail: dongjwen@mail.sysu.edu.cn
[c]Institute of Microscale Optoelectronics, Shenzhen University, Shenzhen 518060, China
[d]Department of Physics and Engineering, ITMO University, Saint Petersburg 197101, Russia
[e]Photonics Initiative, Advanced Science Research Center, City University of New York, New York NY 10031, USA
†Electronic supplementary information (ESI) available. See DOI: 10.1039/d0nr05745b

broadband, wide-angle range and applicable for both transverse electric (TE) and transverse magnetic (TM) polarizations. Thanks to the structural simplicity of such inclusions, an arbitrary phase profile can be continuously modulated through a displacement-varying detour phase scheme, which was experimentally demonstrated by a visible light hologram with extreme angle/wavelength/polarization tolerance. Compared with widely explored gradient metasurfaces and traditional binary optics that modulate phase of wavefront with discrete multiple or binary levels, our proposed metagratings open a new route towards high-efficiency light wavefront shaping with continuous modulation and alleviated structural complexity, making mass production feasible for use in daily life based on low-cost fabrication techniques such as nano-imprinting.

Fig. 1a shows the schematic of the proposed metagrating, made up of silicon nitride (SiN_x) nanobars with width w, height h, periodicity p and refractive index n_g on top of a silicon dioxide (SiO_2) substrate with refractive index n_s. The allowed radiative diffraction orders of the metagrating can be described by a diffraction order chart under the semi-infinite substrate approximation as shown in Fig. 1b,[31] which is constructed by a series of transmission Wood anomaly[55] (TWA, blue) lines and reflection Wood anomaly (RWA, red) lines, determined by

$$k_x \pm i2\pi/p = \pm k_0, \quad (1)$$
$$k_x \pm i2\pi/p = \pm n_s k_0, \quad (2)$$

respectively, where $k_0 = \omega/c$ is the wavevector of the incident light in a vacuum, k_x is the x-component wavevector, and $\pm i^{th}$ (i

= 0, 1, 2, ...) denotes the order of those Wood anomaly lines. We can locate a pair of diffractive regimes denoted by the dotted shadow areas, where only the 0th and -1st diffraction channels in both transmission (T_0, T_{-1}) and reflection sides (R_0, R_{-1}) are allowed. The left target regime is delimited by the 0th TWA, 2nd RWA, -1st RWA and 1st TWA, and the right target regime is delimited by the 0th TWA, -2nd RWA, 1st RWA and -1st TWA, respectively. In such a few-diffraction-order grating configuration, proper engineering of the interference of the multipole modes supported by the SiN_x nanobars enables full transmission of the incident light towards a diffraction order of choice, including negative refraction towards the T_{-1} diffraction direction, as shown in Fig. 1a. In order to then realize arbitrary wavefront shaping at this diffraction order, we can further modulate the metagrating using an interferometric fringe profile,[27,56] as shown in Fig. 1c. This is achieved by exploiting the interference phase difference between adjacent nanobars originating from the light path difference between the incident side $d_i(x,y) = d(x,y)\sin\theta_0$ and the one in the transmission side $d_t(x,y) = d(x,y)\sin\theta_{-1}$ (Fig. 1d). Combined with the grating equation $k_0(\sin\theta_0 + \sin\theta_{-1}) = 2\pi/p$, the modulated phase profile is then given by

$$\varphi(x,y) = k_0(d_i + d_t) = 2\pi d(x,y)/p, \quad (3)$$

where d is the shifted displacement of the SiN_x nanobar from its original periodic position, and p is the periodicity of the metagrating. Note that, eqn (3) is derived without considering the actual inclusion of the metagrating and is independent of
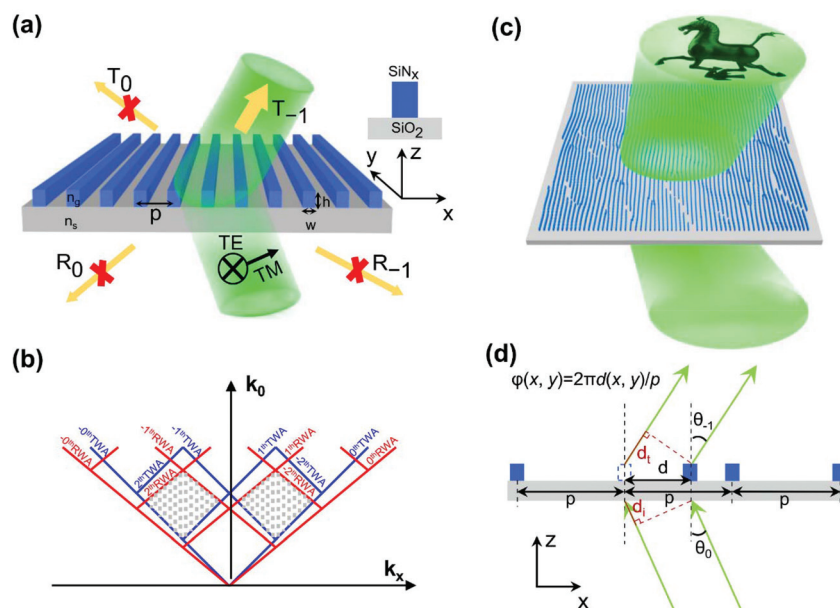

Fig. 1 Schematic of a CMOS-compatible SiN_x metagrating. (a) The metagrating is composed of SiN_x nanobars with refractive index n_g, width w, height h, and periodicity p on top of a SiO_2 substrate with refractive index n_s, working in the diffraction regime that supports the 0th and -1st diffraction channels in both reflection (R_0, R_{-1}) and transmission (T_0, T_{-1}) spaces. After proper optimization, only the T_{-1} channel is allowed, with complete suppressions of T_0, R_0 and R_{-1}. (b) Diffraction order chart showing a series of transmissive Woods anomaly (TWA) lines (blue) and reflective Woods anomaly (RWA) lines (red). The gray dotted areas represent the working regimes for near-unitary diffraction. (c) Continuously modulated diffraction metagratings can perform high-efficiency wavefront shaping in the visible range. (d) Phase modulation rule for arbitrary wavefront shaping in diffraction metagratings.

incident angle, wavelength and polarization, and thus it is applicable for arbitrarily shaped metagratings. The nearfield coupling between adjacent nanobars only affect the diffraction efficiency, but not the modulated phase. Compared with traditional binary optics that modulates the phase with only two levels (0 and π), our proposed metagrating is able to continuously modulate the phase profile by continuously shifting the nanobars, although the structure still manifests a binary geometric profile along the vertical direction.

The ideal perfect diffraction can be achieved by a freestanding metagrating as shown in ESI Fig. 1.† As we can see, the perfect transmission diffraction in the -1st order can be achieved with unitary efficiency $T_{-1} = 100\%$, while all other diffraction channels (R_0, R_{-1}, and T_0) are completely suppressed. Multipolar[54,57] interactions in the supported metagrating may lead to the desired destructive interferences among different diffraction orders and finally form the single channel diffraction. High diffraction efficiencies of the metagrating are robust for a large bandwidth of about 100 nm and large angle range from 15 to 50 degrees at half maximum for both TE and TM polarizations (ESI Fig. S2†). Furthermore, as demonstrated in ESI Fig. S3,† the peak diffraction efficiencies sustain high values for a large range of the nanobar width and height, indicating that the metagrating performance is immune to geometric imperfections, which relaxes the fabrication demand and facilitates the practical implementation significantly. As the SiN_x material has a moderate refractive index and supports low-quality-factor resonances so that the dispersionless localized mode is weakly confined within those nanobars, broadband and wide-angle performance are possible to be achieved in the metagrating. In addition, for both polarizations, similar multipole resonance contributions are supported under the same nanobar parameters (ESI Fig. S2†), which leads to the polarization tolerance.

The inclusion simplicity of the SiN_x metagrating allows for arbitrary wavefront shaping based on the detour phase approach relying on the displacements of nanobars. As an example, we modulate the SiN_x metagrating to demonstrate a hologram in the full visible range (ESI Fig. S4†). The phase profile of a horse image was calculated by the Gerchberg–Saxton (GS) algorithm[58] as shown in ESI Fig. S3a.† We discretize the nanobars in the y-direction with period $p_y = 300$ nm, so that the each element of the metagrating hologram can be seen as a finite length nanobar with width w, height h and length p_y. Based on the displacement encoding approach denoted in Fig. 1c, we can modulate the phase profile continuously by moving the unit-element in each period, resulting in a curved grating profile (ESI Fig. S4b†), which is similar to an interferometric fringe between the object wave and the reference plane wave. Note that, to avoid the near-field coupling induced efficiency difference and also the fabrication difficulty, in the practical design of the metagrating hologram, we set a minimum spacing of 80 nm, below which one of the nanobars will be deleted. The overall deleted nanobars are below 1% so that the overall modulated wavefront is hardly affected. Resorting to an angle-resolved optical setup (Fig. 2a),
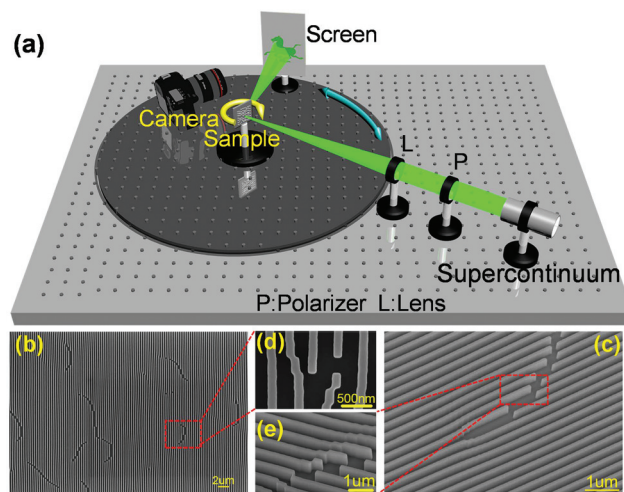
Fig. 2 Experimental realization of the SiN_x metagrating hologram with continuous phase modulation. (a) Angle-resolved optical setup for the wide-angle full visible range holographic imaging. (b–e) SEM images of the continuously modulated SiN_x metagratings on the top view (b and d), and the oblique view (c and e).

we can capture holographic images by varying both wavelengths and incident angles of the modulated metagrating. To experimentally realize the metagrating, we use the experimentally obtained material parameters of SiN_x (ESI Fig. S8†) and also consider the substrate to recalculate the optimized parameters. The determined parameters for realistic metagratings are $w = 150$ nm, $h = 300$ nm, $p = 400$ nm, and $n_s = 1.5$, of which the bandwidth and angle range are both broad in the visible range, although the peak diffraction efficiency cannot perfectly achieve 100% in the practical situation due to scattering loss and the presence of the substrate (Fig. 4a–d). The metagrating based on the above parameters and the holographic phase modulation given by eqn (3) was fabricated by electron beam lithography (EBL) following the process described in ESI Fig. S5.† The fabricated metagrating sample in both top (Fig. 2b and d) and oblique views (Fig. 2c and e) manifests continuously curved SiN_x segments with perfect steep flank profile, well matching the theoretically designed shapes.

Fig. 3 shows the experimentally reconstructed holographic images over nearly the full metagrating work regime as indicated in Fig. 1b for TE polarizations. The incident angle spans over 10°–80° and the incident wavelength spans nearly the full visible range (450 nm–700 nm) for both TE and TM polarizations. The holographic image sizes are different for different colors, according to the scaling factor λ/z_d (λ is the wavelength in free space and z_d is the distance between the image and the hologram plane). For clarity, we just show the minimum picture ranges containing the horse image, abandoning their relative size information. It is clear that all the reconstructed images have high fidelity over the full visible band and for a broad angular range, except those angles beyond the cut-off angle of the metagrating regime (right-lower corner of Fig. 3), which corresponds to the -1th TWA lines in Fig. 1b. The holo-
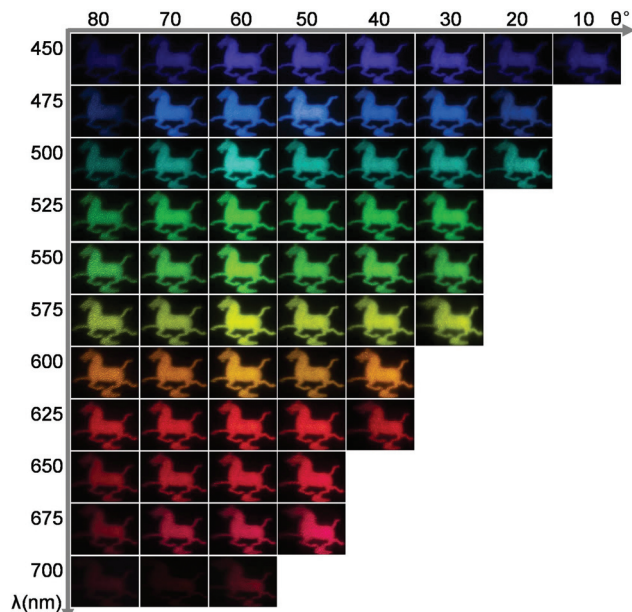
Fig. 3 Experimentally reconstructed holographic images of the modulated metagrating acquired at different incident angles and different wavelenths in the full visible spectrum. The illumination light is TE polarized.

graphic images span over all colors, including purple, blue, cyan, green, yellow, orange and red. Although the images close to the boundary are a little blurred and stretched due to the reduced diffraction efficiency and enlarged diffraction beam width, high-fidelity holographic images can be preserved at most angles and wavelengths. The comparison of reconstructed holographic images for TE and TM polarizations are shown in ESI Fig. S7,† manifesting excellent polarization tolerances.

The diffraction efficiencies of the experimentally realized metagratings are analyzed and shown in Fig. 4. Fig. 4a–d show the calculated diffraction efficiencies of the periodic SiN_x metagrating considering the experimentally obtained material parameters (ESI Fig. S8†) and the same unit-cell parameters as those of the fabricated phase-modulated metagrating. Fig. 4e–h show the measured diffraction efficiencies for the fabricated phase-modulated metagrating. For TE polarization (Fig. 4c and e), the calculated diffraction efficiency of T_{-1} shows a broad bandwidth of operation, from 470 nm to 730 nm, spanning the entire visible range, with a peak efficiency of 93%. The measured efficiency has a peak value of 75% with nearly the same bandwidth compared with the calculated one. For TM polarization (Fig. 4d and f), the peak diffraction efficiency reaches 87% in theory and 65% in experiment, with a smaller bandwidth from 470 nm to 600 nm. For both polarizations, although the measured absolute diffraction efficiencies are a little lower than the calculated ones due to the scattering loss of the fabricated structure that is inevitably deviated from the ideally designed structure, the overall diffraction spectra are in general consistent with the simulation results. Fig. 4g and h show the diffraction efficiency (T_{-1}) evolution with incident angles. The measured efficiencies exhibit flat-top peaks against incident angles and, at middle wavelengths around 500 nm, the angular bandwidth is the largest, covering the incident angle range from 20° to 80°. Note that the incident angle θ_0 is taken in the air region below the substrate in experiments, while in calculation, the incident light is directly from the substrate region. According to Snell's law, the grazing incident angle $\theta_0 = 90°$ in air corresponds to $\theta'_0 = 41.8°$ in the substrate. Therefore, the calculated diffraction efficiencies do not decline at the air angle $\theta_0 = 90°$ (Fig. 4a and b), while the measured diffraction efficiencies decline when $\theta_0 > 70°$ because at such a large incidence angle, the light spot size is far larger than the sample size and the coupled light from the air to the substrate is dramatically reduced.
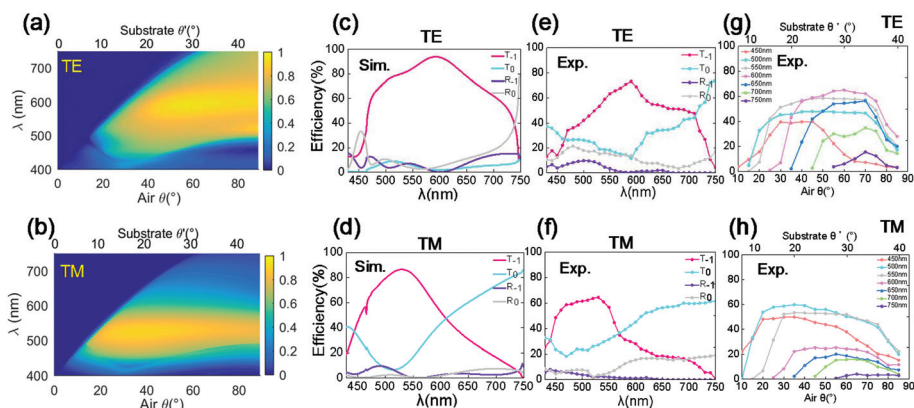
Fig. 4 Comparison of diffraction spectra of theoretically modeled periodical SiN_x metagrating and experimentally realized phase-modulated SiN_x metagrating based on the same parameter sets: w = 150 nm, h = 300 nm, p = 400 nm, and n_s = 1.5. (a and b) Calculated diffraction efficiency map for varying incident angles and wavelengths of the periodic SiN_x metagrating, (a) for TE polarization and (b) for TM polarization, respectively. (c and d) Calculated efficiency spectra of various diffraction orders (T_{-1}, T_0, R_{-1}, and R_0) at 60° incident angle from air, for the periodic metagrating, for (c) TE polarization and (d) TM polarization. (e–h) Experimental measurement of diffraction efficiencies of the realized phase-modulated metagrating in Fig. 3 for different wavelengths and incident angles, at (e and g) TE and (f and h) TM polarization illumination, respectively.

In summary, we have put forward a highly efficient all-dielectric metagrating formed by rectangular profiles with neither high index nor high aspect ratio requirement, and further experimentally demonstrated its continuous phase modulation capability using the CMOS-compatible SiN_x platform. Unitary diffraction efficiency can be in principle achieved in transmission mode, with complete suppression of all specular and higher diffraction orders. Simple inclusion of the metagrating enables arbitrary wavefront shaping through a displacement-varying detour phase scheme for advanced applications. High diffraction efficiency meta-hologram with continuously modulated phase profile was realized, demonstrating large angle/wavelength/polarization tolerance. Our findings open new routes to high-efficiency wavefront shaping with analog modulation and relaxed fabrication demands, hopefully making mass production of high-efficiency meta-holograms for daily life usage feasible.

Methods

Theoretical analysis and numerical simulations

The theoretical analysis of the perfect diffraction metagrating with a fixed refractive index was performed by RCWA implemented by an open source Matlab program Reticolo and multipole expansion method. The numerical simulation of diffraction efficiencies of multiple diffraction orders of the realistic SiN_x metagratings with experimentally obtained material parameters was conducted by the FEM method implemented by COMSOL Multiphysics.

Experimental samples and measurements

The metagrating was fabricated on a silicon dioxide substrate. First, a layer of 300 nm thick SiN_x film was deposited on the substrate using an inductively coupled plasma-chemical vapor deposition (ICP-CVD) system (Plasmalab System 100 ICP180, Oxford). Next, the metagrating pattern was generated in the high-resolution positive resist (ZEP520A) using an electron-beam lithography (EBL) system (Vistec EBPG5000 ES) at 100 kV. Next, the reactive-ion-etch (RIE) (Oxford Instrument Plasmalab System 100 RIE180) with a mixture of CHF_3 and O_2 gases was used to transfer the pattern down to the SiN_x layer. The whole process for the metagrating fabrication is shown in ESI Fig. S5† in detail. In the experimental measurement, a supercontinuum laser source was employed to illuminate the metagrating with varying incident angles. The diffracted holographic image was shown on a white screen and captured using a Nikon camera (Fig. 2a). The diffraction efficiencies for varying incident angles and varying wavelengths were obtained by collecting the power of those holographic images into a power meter (ESI Fig. S6†).

Author contributions

Z.-L. D. initiated the idea and made the theoretical analysis. X. Y. and Z.-L. D. carried out the simulations. X. Y., Q.-A. T., H.-Y. Q., and Z.-P. Z. conducted the experiment measurement with the help of Z.-L. D and T. S. The sample was fabricated by H.-Y. Q., Z.-P. Z., and J.-W. D. Z.-L. D., X. Y., J.-W. D., and X. L. analyzed the data. Z.-L. D. wrote the manuscript with input from X. Y., J.-W. D., Y. C., B.-O. G., N. F., G. P. W., P. K., A. A., and X. L. All authors contributed to discussions about the manuscript.

Conflicts of interest

The authors declare no conflicts of interest.

Acknowledgements

References

1 P. Genevet, F. Capasso, F. Aieta, M. Khorasaninejad and R. Devlin, *Optica*, 2017, **4**, 139–152.

2 D. Lin, P. Fan, E. Hasman and M. L. Brongersma, *Science*, 2014, **345**, 298–302.

3 M. Khorasaninejad, W. T. Chen, R. C. Devlin, J. Oh, A. Y. Zhu and F. Capasso, *Science*, 2016, **352**, 1190–1194.

4 E. Arbabi, A. Arbabi, S. M. Kamali, Y. Horie and A. Faraon, *Optica*, 2016, **3**, 628–633.

5 A. Arbabi, Y. Horie, M. Bagheri and A. Faraon, *Nat. Nanotechnol.*, 2015, **10**, 937–943.

6 J. P. Balthasar Mueller, N. A. Rubin, R. C. Devlin, B. Groever and F. Capasso, *Phys. Rev. Lett.*, 2017, **118**, 113901.

7 Z.-L. Deng, S. Zhang and G. P. Wang, *Opt. Express*, 2016, **24**, 23118–23128.

8 W. T. Chen, A. Y. Zhu, V. Sanjeev, M. Khorasaninejad, Z. Shi, E. Lee and F. Capasso, *Nat. Nanotechnol.*, 2018, **13**, 220–226.

9 S. Wang, P. C. Wu, V.-C. Su, Y.-C. Lai, M.-K. Chen, H. Y. Kuo, B. H. Chen, Y. H. Chen, T.-T. Huang, J.-H. Wang, R.-M. Lin, C.-H. Kuan, T. Li, Z. Wang, S. Zhu and D. P. Tsai, *Nat. Nanotechnol.*, 2018, **13**, 227–232.

10 P. Lalanne and P. Chavel, *Laser Photonics Rev.*, 2017, **11**, 1600295.

11 G. Zheng, H. Mühlenbernd, M. Kenney, G. Li, T. Zentgraf and S. Zhang, *Nat. Nanotechnol.*, 2015, **10**, 308–312.

12 L. Wang, S. Kruk, H. Tang, T. Li, I. Kravchenko, D. N. Neshev and Y. S. Kivshar, *Optica*, 2016, **3**, 1504–1505.

13 Z.-L. Deng, M. Jin, X. Ye, S. Wang, T. Shi, J. Deng, N. Mao, Y. Cao, B.-O. Guan, A. Alù, G. Li and X. Li, *Adv. Funct. Mater.*, 2020, **30**, 1910610.

14 P. Yu, J. Li, S. Zhang, Z. Jin, G. Schütz, C.-W. Qiu, M. Hirscher and N. Liu, *Nano Lett.*, 2018, **18**, 4584–4589.

15 Y. Hu, L. Li, Y. Wang, M. Meng, L. Jin, X. Luo, Y. Chen, X. Li, S. Xiao, H. Wang, Y. Luo, C.-W. Qiu and H. Duan, *Nano Lett.*, 2020, **20**, 994–1002.

16 L. Jin, Z. Dong, S. Mei, Y. F. Yu, Z. Wei, Z. Pan, S. D. Rezaei, X. Li, A. I. Kuznetsov, Y. S. Kivshar, J. K. W. Yang and C.-W. Qiu, *Nano Lett.*, 2018, **18**, 8016–8024.

17 L. Jin, Y.-W. Huang, Z. Jin, R. C. Devlin, Z. Dong, S. Mei, M. Jiang, W. T. Chen, Z. Wei, H. Liu, J. Teng, A. Danner, X. Li, S. Xiao, S. Zhang, C. Yu, J. K. W. Yang, F. Capasso and C.-W. Qiu, *Nat. Commun.*, 2019, **10**, 4789.

18 J. Li, Y. Chen, Y. Hu, H. Duan and N. Liu, Magnesium-Based Metasurfaces for Dual-Function Switching between Dynamic Holography and Dynamic Color Display, *ACS Nano*, 2020, **14**(7), 7892–7898.

19 Z. Li, I. Kim, L. Zhang, M. Q. Mehmood, M. S. Anwar, M. Saleem, D. Lee, K. T. Nam, S. Zhang, B. Luk'yanchuk, Y. Wang, G. Zheng, J. Rho and C.-W. Qiu, *ACS Nano*, 2017, **11**, 9382–9389.

20 A. Nemati, Q. Wang, M. Hong and J. Teng, *Opto-Electron. Adv.*, 2018, **1**, 180009.

21 A. M. Shaltout, V. M. Shalaev and M. L. Brongersma, *Science*, 2019, **364**, eaat3100.

22 L. Cao, P. Fan, E. S. Barnard, A. M. Brown and M. L. Brongersma, *Nano Lett.*, 2010, **10**, 2649–2654.

23 D. Wen, J. J. Cadusch, J. Meng and K. B. Crozier, *Adv. Funct. Mater.*, 2020, **30**, 1906415.

24 S. Sun, Z. Zhou, C. Zhang, Y. Gao, Z. Duan, S. Xiao and Q. Song, *ACS Nano*, 2017, **11**, 4445–4452.

25 Y. Ra'di, D. L. Sounas and A. Alù, *Phys. Rev. Lett.*, 2017, **119**, 067404.

26 Z.-L. Deng, S. Zhang and G. P. Wang, *Nanoscale*, 2016, **8**, 1588–1594.

27 Z.-L. Deng, J. Deng, X. Zhuang, S. Wang, T. Shi, G. P. Wang, Y. Wang, J. Xu, Y. Cao, X. Wang, X. Cheng, G. Li and X. Li, *Light: Sci. Appl.*, 2018, **7**, 78.

28 N. M. Estakhri, V. Neder, M. W. Knight, A. Polman and A. Alù, *ACS Photonics*, 2017, **4**, 228–235.

29 Y. Ra'di and A. Alù, *ACS Photonics*, 2018, **5**, 1779–1785.

30 A. M. H. Wong and G. V. Eleftheriades, *Phys. Rev. X*, 2018, **8**, 011036.

31 Z.-L. Deng, Y. Cao, X. Li and G. P. Wang, *Photonics Res.*, 2018, **6**, 443–450.

32 A. Epstein and O. Rabinovich, *Phys. Rev. Appl.*, 2017, **8**, 054037.

33 V. Popov, F. Boust and S. N. Burokur, *Phys. Rev. Appl.*, 2018, **10**, 011002.

34 V. Popov, M. Yakovleva, F. Boust, J.-L. Pelouard, F. Pardo and S. N. Burokur, *Phys. Rev. Appl.*, 2019, **11**, 044054.

35 Z.-L. Deng, J. Deng, X. Zhuang, S. Wang, K. Li, Y. Wang, Y. Chi, X. Ye, J. Xu, G. P. Wang, R. Zhao, X. Wang, Y. Cao, X. Cheng, G. Li and X. Li, *Nano Lett.*, 2018, **18**, 2885–2892.

36 S. Wang, F. Li, J. Deng, X. Ye, Z.-L. Deng, Y. Cao, B.-O. Guan, G. Li and X. Li, *J. Phys. D: Appl. Phys.*, 2019, **52**, 324002.

37 M. Li, L. Jing, X. Lin, S. Xu, L. Shen, B. Zheng, Z. Wang and H. Chen, *Adv. Opt. Mater.*, 2019, **7**, 1900151.

38 M. Khorasaninejad and F. Capasso, *Nano Lett.*, 2015, **15**, 6709–6715.

39 E. Khaidarov, H. Hao, R. Paniagua-Domínguez, Y. F. Yu, Y. H. Fu, V. Valuckas, S. L. K. Yap, Y. T. Toh, J. S. K. Ng and A. I. Kuznetsov, *Nano Lett.*, 2017, **17**, 6267–6272.

40 D. Sell, J. Yang, S. Doshay, R. Yang and J. A. Fan, *Nano Lett.*, 2017, **17**, 3752–3757.

41 Z. Fan, M. R. Shcherbakov, M. Allen, J. Allen, B. Wenner and G. Shvets, *ACS Photonics*, 2018, **5**, 4303–4311.

42 T. Shi, Y. Wang, Z.-L. Deng, X. Ye, Z. Dai, Y. Cao, B.-O. Guan, S. Xiao and X. Li, *Adv. Opt. Mater.*, 2019, 7(24), 1901389.

43 D. Sell, J. Yang, E. W. Wang, T. Phan, S. Doshay and J. A. Fan, *ACS Photonics*, 2018, **5**, 2402–2407.

44 J. Jiang, D. Sell, S. Hoyer, J. Hickey, J. Yang and J. A. Fan, *ACS Nano*, 2019, **13**, 8872–8878.

45 D. Lin, M. Melli, E. Poliakov, P. S. Hilaire, S. Dhuey, C. Peroz, S. Cabrini, M. Brongersma and M. Klug, *Sci. Rep.*, 2017, **7**, 2286.

46 X. Dong, J. Cheng, F. Fan and S. Chang, *Opt. Lett.*, 2019, **44**, 939–942.

47 A. Casolaro, A. Toscano, A. Alù and F. Bilotti, *IEEE Trans. Antennas Propag.*, 2020, **68**, 1542–1552.

48 O. Rabinovich and A. Epstein, *IEEE Trans. Antennas Propag.*, 2020, **68**, 1553–1568.

49 R. Paniagua-Domínguez, Y. F. Yu, E. Khaidarov, S. Choi, V. Leong, R. M. Bakker, X. Liang, Y. H. Fu, V. Valuckas, L. A. Krivitsky and A. I. Kuznetsov, *Nano Lett.*, 2018, **18**, 2124–2132.

50 Y. Fu, C. Shen, Y. Cao, L. Gao, H. Chen, C. T. Chan, S. A. Cummer and Y. Xu, *Nat. Commun.*, 2019, **10**, 2326.

51 B. W. Shore, M. D. Perry, J. A. Britten, R. D. Boyd, M. D. Feit, H. T. Nguyen, R. Chow, G. E. Loomis and L. Li, *J. Opt. Soc. Am. A*, 1997, **14**, 1124–1136.

52 J. Du, Z. Lin, S. T. Chui, W. Lu, H. Li, A. Wu, Z. Sheng, J. Zi, X. Wang, S. Zou and F. Gan, *Phys. Rev. Lett.*, 2011, **106**, 203903.

53 A. Wu, H. Li, J. Du, X. Ni, Z. Ye, Y. Wang, Z. Sheng, S. Zou, F. Gan, X. Zhang and X. Wang, *Nano Lett.*, 2015, **15**, 2055–2060.

54 W. Liu and A. E. Miroshnichenko, *ACS Photonics*, 2018, **5**, 1733–1741.

55 J. E. Stewart and W. S. Gallaway, *Appl. Opt.*, 1962, **1**, 421–430.

56 Z. Xie, T. Lei, G. Si, X. Wang, J. Lin, C. Min and X. Yuan, *ACS Photonics*, 2017, **4**, 2158–2164.

57 P. Grahn, A. Shevchenko and M. Kaivola, *New J. Phys.*, 2012, **14**, 093033.

58 X. Li, H. Ren, X. Chen, J. Liu, Q. Li, C. Li, G. Xue, J. Jia, L. Cao, A. Sahu, B. Hu, Y. Wang, G. Jin and M. Gu, *Nat. Commun.*, 2015, **6**, 6984.